Inorganic Chemistry

Article

pubs.acs.org/IC

Copper-Organic/Octamolybdates: Structures, Bandgap Sizes, and Photocatalytic Activities

Lan Luo, Haisheng Lin, Le Li, Tatyana I. Smirnova, and Paul A. Maggard*

Department of Chemistry, North Carolina State University, Raleigh, North Carolina 27695-8204, United States

Supporting Information

ABSTRACT: The structures, optical bandgap sizes, and photocatalytic activities are described for three copper–octamolybdate hybrid solids prepared using hydrothermal methods, $[Cu(pda)]_4[\beta\text{-}Mo_8O_{26}]$ (**I**; pda = pyridazine), $[Cu(en)_2]_2[\gamma\text{-}Mo_8O_{26}]$ (**II**; en = ethylenediamine), and $[Cu(o\text{-}phen)_2]_2[\alpha\text{-}Mo_8O_{26}]$ (**III**; *o*-phen = *o*-phenanthroline). The structure of **I** consists of a $[Cu(pda)]_4^{4+}$ tetramer that bridges to neighboring $[\beta\text{-}Mo_8O_{26}]^{4-}$ octamolybdate clusters to form two-dimensional layers that stack along the *a* axis. The previously reported structures of **II** and **III** are constructed from $[Cu_2(en)_4Mo_8O_{26}]$ and $[Cu_2(o\text{-}phen)_4Mo_8O_{26}]$ clusters. The optical bandgap sizes were measured by UV–vis diffuse reflectance techniques to be ∼1.8 eV for **I**, ∼3.1 eV for **II**, and ∼3.0 eV for **III**. Electronic structure calculations show that the smaller bandgap size of **I** originates primarily from an electronic transition between the valence and conduction band edges comprised of filled $3d^{10}$ orbitals on Cu(I) and empty $4d^0$ orbitals on Mo(VI). Both **II** and **III** contain Cu(II) and exhibit larger bandgap sizes. Accordingly, aqueous suspensions of **I** exhibit visible-light photocatalytic activity for the production of oxygen at a rate of ∼90 μmol O_2 g^{-1} h^{-1} (10 mg samples; radiant power density of ∼1 W/cm^2) and a turnover frequency per calculated surface $[Mo_8O_{26}]^{4-}$ cluster of ∼36 h^{-1}. Under combined ultraviolet and visible-light irradiation, **I** also exhibits photocatalytic activity for hydrogen production in 20% aqueous methanol of ∼316 μmol H_2 g^{-1} h^{-1}. By contrast, **II** decomposed during the photocatalysis measurements. The molecular $[Cu_2(o\text{-}phen)_4(\alpha\text{-}Mo_8O_{26})]$ clusters of **III** dissolve into the aqueous methanol solution under ultraviolet irradiation and exhibit homogeneous photocatalytic rates for hydrogen production of up to ∼8670 μmol $H_2{\cdot}g^{-1}$ h^{-1} and a turnover frequency of 17 h^{-1}. The clusters of **III** can be precipitated out by evaporation and redispersed into solution with no apparent decrease in photocatalytic activity. During the photocatalysis measurements, the dissolution of the clusters in **III** is found to occur with the reduction of Cu(II) to Cu(I), followed by subsequent detachment from the octamolybdate cluster. The lower turnover frequency, but higher photocatalytic rate, of **III** arises from the net contribution of all dissolved $[Cu_2(o\text{-}phen)_4(\alpha\text{-}Mo_8O_{26})]$ clusters, compared to only the surface clusters for the heterogeneous photocatalysis of **I**.

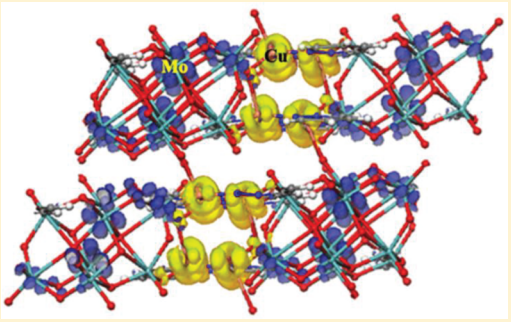

INTRODUCTION

Investigations into new inorganic materials for driving photocatalytic water-splitting reactions, i.e., for the production of hydrogen and oxygen, have drawn intense research attention in recent years.[1−4] While numerous metal oxides exhibit high photocatalytic activities, most of these are active under only ultraviolet-light irradiation. It has proven challenging to lower their bandgap sizes in order to absorb a greater fraction of incoming sunlight, while also possessing high stability and efficient photocatalytic activity for water oxidation and reduction. Inorganic materials containing a combination of early transition-metal cations (e.g., Ta(V) or Mo(VI)) with late transition-metal cations (e.g., Cu(I), Ag(I)) have shown a significant red-shifting of their bandgap sizes to visible-light energies owing to a metal-to-metal charge transfer between the d^{10} and d^0 electron configurations. Examples include several recently reported Cu(I) niobates and Cu(I) tantalates, such as $CuNbO_3$, $CuNb_3O_8$, and $Cu_5Ta_{11}O_{30}$,[5−9] which exhibit high cathodic photocurrents as p-type polycrystalline films.

The addition of coordinating organic ligands within the structures of metal oxides, i.e., in the synthesis of metal-oxide/organic hybrids, enables a finer molecular-level control over their structures and properties.[10,11] Within this research field, our group has discovered some of the first photocatalytically active hybrid materials based on $[Ag(L)]^+$ (L = organic ligand) networks combined with vanadate or niobium oxyfluoride building blocks, e.g., $Ag(pyz)NbOF_4$ (pyz = pyrazine) and $Ag_4(pzc)_2V_2O_6$ (pzc = pyrazinecarboxylate).[12,13] Their photocatalytic activities have so far remained limited to the decomposition of the methylene blue dye molecule under ultraviolet irradiation. In related hybrid systems, recent research has demonstrated that structures containing various types of polyoxomolybdate clusters, e.g., $[Mo_{10}O_{34}]^{8-}$, $[Mo_6O_{19}]^{2-}$, and $[Mo_8O_{26}]^{4-}$, can exhibit heterogeneous photocatalytic activity for the decomposition of methylene blue under ultraviolet irradiation.[14−16] When dissolved in solution, several types of

Received: November 23, 2013
Published: March 7, 2014

   dx.doi.org/10.1021/ic402910a | *Inorg. Chem.* 2014, 53, 3464−3470

polyoxomolybdate and polyoxotungstate clusters have been found to catalytically oxidize water to oxygen at high rates (not light driven), such as $[Ru_4(\mu\text{-}O)_4(\mu\text{-}OH)_2(H_2O)_4(\gamma\text{-}SiW_{10}O_{36})_2]^{10-}$ and $[Co_4(H_2O)_2(\alpha\text{-}PW_9O_{34})2]^{10-}$, with turnover frequencies ranging from ~1000 h^{-1} to 18 000 h^{-1}.[17,18] To our knowledge, metal-oxide/organic solids that show heterogeneous photocatalytic activity for the oxidation and reduction of water are currently not well-known.

Our prior investigations into Cu(I)-containing hybrids have revealed many new compounds that exhibit bandgap sizes (E_g) within the visible-light energy range, including $CuReO_4(pyz)$ (E_g ~ 2.5 eV), Cu(bpy)ReO_4 (E_g ~ 2.0 eV), and others.[12,19,20] Similar to the condensed metal-oxides, their relatively smaller bandgap sizes arise from a metal-to-metal charge transfer between the Cu(I) cation and an early transition-metal cation, e.g., Re(VII), Nb(V), or V(V). However, these Cu(I)-containing hybrids have previously not been found to exhibit photocatalytic activity in aqueous solutions. Herein, we report the synthesis of a Cu(I)-containing hybrid with octamolybdate clusters, i.e., $[Cu(pda)]_4[\beta\text{-}Mo_8O_{26}]$ (**I**) (pda = pyridazine), with a visible-light bandgap size and photocatalytic activity for oxygen and hydrogen production. In addition, Cu(II)-containing hybrids with octamolybdate clusters, i.e., $[Cu(en)_2]_2[\gamma\text{-}Mo_8O_{26}]$ (**II**) (en = ethylenediamine) and $[Cu(o\text{-}phen)_2]_2[\alpha\text{-}Mo_8O_{26}]$ (**III**) (*o*-phen = *o*-phenanthroline),[21,22] were investigated in order to understand the effects of structural features the copper oxidation state on their bandgap sizes, photocatalytic activities, and solubility in aqueous solutions.

EXPERIMENTAL SECTION

Materials. All starting reagents were purchased from commercial suppliers and used without further purification, including Cu_2O (99.9% metal basis, Alfa Aesar), $CuCl_2$ (99%, Alfa Aesar), $CuSO_4$ (98.8%, Fisher Scientific), $(NH_4)_2MoO_4$ (99.99% metal basis, Alfa Aesar), MoO_3 (99.998% metal basis excluding W, Alfa Aesar), KOH (≥85.0%, Fisher Scientific), pyridazine (98+%, Alfa Aesar), ethylenediamine dihydrochloride (98%, Aldrich), and *o*-phenanthroline (99+%, Aldrich). A reagent amount of deionized water was also used as solvent in the syntheses.

Synthesis. $[Cu(pda)]_4[\beta\text{-}Mo_8O_{26}]$ (**I**) was prepared via a hydrothermal procedure by heat-sealing all reactants into a polytetrafluoroethylene Teflon pouch, in weighed amounts of 14.4 mg (0.10 mmol) of Cu_2O, 61.8 mg (0.05 mmol) of $(NH_4)_6Mo_7O_{24}\cdot 4H_2O$, 16.0 mg (0.20 mmol) of pyridazine, and 0.20 g (11.1 mmol) of H_2O. The sealed pouches were then placed into an ~125 mL polytetrafluoroethylene-lined stainless steel autoclave that was backfilled with ~40 mL of deionized water before closing. The reactants were heated at 180 °C for 24 h inside a convection oven. Black-red prism crystals of **I** were obtained in ~92% yield based on Cu. A small amount of unidentified fine yellow powder is observed that can be removed by dispersing the product into ~30 mL of water and sonicating for 20−30 s, followed by decanting after the red-colored crystals have been allowed to settle for ~1−2 min. This sonication/separation process was repeated three times until a pure sample of **I** was obtained, as judged by PXRD and visually under a microscope.

$[Cu(en)_2]_2[\gamma\text{-}Mo_8O_{26}]$ (**II**) was prepared by a hydrothermal reaction of a mixture of 0.0175 g of $CuCl_2$, 0.0169 g of MoO_3, 0.0556 g of ethylenediamine dihydrochloride, 0.05 g of KOH, and ~2 mL of H_2O in a molar ratio of 1:1:2:4:~1000 and heated to 150 °C for 48 h in a convection oven. The product formed as large, purple, cubic-shaped crystals that were washed with deionized water without further purification and dried at 60 °C overnight. The product was obtained in high purity (>95%) according to powder X-ray diffraction analysis.

$[Cu(o\text{-}phen)_2]_2[\alpha\text{-}Mo_8O_{26}]$ (**III**) was prepared by a hydrothermal reaction of a mixture of 0.0175 g of $CuSO_4$, 0.0169 g of MoO_3, 0.0390 g of *o*-phenanthroline, and ~2 mL of H_2O in a molar ratio of 1:2:2:~1000. The reactants were heated to 180 °C for 68 h in a convection oven. The products were sonicated and washed with deionized water to separate the green cubic-shaped crystalline products from an unidentified white powder. The product was obtained in high purity (>95%) according to powder X-ray diffraction analysis.

Characterization Methods. A single-crystal X-ray data set for **I** was collected on a Bruker APEX-II CCD diffractometer using graphite-monochromatized Mo Kα radiation (λ = 0.71073 Å) from a sealed tube at 296 K. The initial unit cell determination and data reduction were performed using the Bruker SAINT program.[23] The structure was solved by direct methods, and the structure refinement was performed by full-matrix least-squares methods in SHELXS-97.[24] Hydrogen atoms were placed in idealized positions that were fixed to ride on the parent carbon or oxygen atoms. Crystallographic data and structure refinement parameters for **I** are given in Table S1 of the Supporting Information. Selected interatomic distances, angles, and bond valences can be found in Table S2 of the Supporting Information.

All powder X-ray diffraction data sets were collected using a high-resolution Rigaku R-Axis Spider powder X-ray diffractometer (graphite monochromatized Cu Kα radiation) at room temperature. The diffraction patterns were scanned with a step size of 0.02° over the 2θ angular range from 4° to 100°. Mid-infrared (400−4000 cm^{-1}) spectra were measured using an IR-Prestige 21 Shimadzu Fourier Transform Infrared (FTIR) Spectrophotometer with sample stage and a GladiATR accessory. X-ray photoelectron spectroscopy data were taken with a Riber MAC2 XPS system. The binding energies were internally calibrated to the graphite C 1s peak at 284.3 eV. Solution samples were investigated by MALDI-TOF/TOF-Mass Spectrometry analyses using an AB SCIEX TOF/TOF 5800 instrument (AB SCIEX, Foster City, CA). The instrument was equipped with a Nd:YAG laser (349 nm wavelength, 3 ns pulse width, 1000 Hz firing rate). The instrument was calibrated in positive linear ion mode using the Cal-1 mixture. The spectra were acquired in positive linear ion mode, with a mass range of 450−1200 *m*/*z*. Mass spectra from 200 laser shots were averaged to produce a composite spectrum. Electrospray ionization mass spectrometry in negative ion mode was performed on a Thermo Fisher Scientific TSQ Quantum Discovery MAX Triple Quadrupole MS instrument equipped with a capillary electrospray (ESI) source via direct injection, with a mass range of 300−1200 *m*/*z*. Thermogravimetric analyses were taken on a TA Instruments TGA Q50. Specific surface areas were measured on a Quantachrome ChemBET Pulsar TPR/TPD. EPR spectra were taken on both solid and solution samples at the X-band frequency with a Bruker Elexsys E500 spectrometer at room temperature. Each solution sample was sealed in a 25 μL quartz capillary. Each solid sample was placed onto a piece of weighing paper that was then folded into a 3 mm × 3 mm square. These were then placed into a 3 mm quartz EPR tube for analysis.

Optical Properties and Photocatalytic Activities. UV−vis diffuse reflectance spectra (DRS) were collected on a Shimadzu UV-3600/3100 UV−vis-NIR spectrophotometer with an integrating sphere. A pressed barium sulfate powder was used as the reference. According to the Kubelka−Munk theory of diffuse reflectance, the data were transformed using the function $F(R_\infty) = (1 - R_\infty)^2/(2R_\infty)$ versus energy, where R_∞ is diffuse reflectance.[25] The data were plotted in the form of Tauc plots as $[F(R) \times h\upsilon]^n$ versus $h\upsilon$, where n = 2 for direct transitions and n = 1/2 for indirect transitions. The optical bandgap sizes were estimated from the onset of absorption, as extrapolated from the linear rising section of the curve that intersects with the baseline.[26]

The photocatalytic activity for hydrogen production was measured by suspending a weighed amount (~5−10 mg typically) of each powdered sample (either pure or coated with 1% platinum) in an outer-irradiation quartz reaction cell that was filled with 45 mL of either deionized water or a 20% aqueous methanol solution.[27] To remove any trapped gases on the particles' surfaces, the particle suspension was first stirred in the dark for ~0.5 h with constant nitrogen bubbling. The cell was then irradiated under a 1000 W high-pressure Xe arc lamp (Newport Oriel 6271, focused through a shutter

dx.doi.org/10.1021/ic402910a | Inorg. Chem. 2014, 53, 3464−3470

window) that was equipped with a water filter and with cutoff filters to select the desired wavelength range. The solutions were irradiated under both UV and visible light ($\lambda > 200$ nm) or only visible light ($\lambda > 420$ nm) with stirring, at a radiant power density of ~1 W/cm^2. Photocatalytic activities were also measured under simulated solar light using an air mass filter (AM 1.5 direct, Newport), specifically for **I** and **III** in deionized water and a 20% aqueous methanol solution. The lamp power was adjusted to ~0.1 W/cm^2 by a radiant power meter in order to simulate the solar flux at the earth's surface.

The photoreaction cell was connected to an L-shaped horizontal quartz tube through an airtight rubber tubing to collect the evolved gas. By injecting a mobile water bubble into the L-shaped tube, the amount of gas produced at a constant pressure can be determined volumetrically by marking its movement every 30 min during the photocatalytic testing experiments. This change in gas volume can be converted into the micromole of gas generated to calculate the hydrogen or oxygen production rate. The collected gas was manually injected into a gas chromatograph (SRI MG #2; thermal conductivity detector) for identification.

Electronic Structure Calculations. Electronic structure calculations were carried out within the commercial software package CASTEP using plane-wave density functional theory.[28] The lattice dimensions and atomic positions were obtained from the respective single crystal structures. The Perdew–Burke–Ernzerhof functional in the generalized gradient approximation and ultrasoft core potentials were utilized in the calculations.[29] Equally distributed *k*-points within the Brillouin zone were automatically calculated based on the Monkhorst–Pack scheme.[30]

RESULTS AND DISCUSSION

Structural Descriptions. The crystalline structure of $[Cu(pda)]_4[\beta\text{-}Mo_8O_{26}]$ (**I**) consists of an equimolar ratio of $[Mo_8O_{26}]^{4-}$ octamolybdate clusters (β-isomer) and $[Cu(pda)]_4^{4+}$ tetramers, shown in Figure 1. The octamolybdate

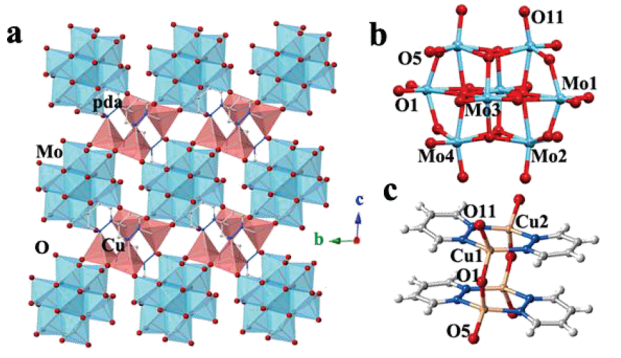

Figure 1. Polyhedral view of **I** (a); blue polyhedra are Mo-centered and pink are Cu-centered. The local structure of $[\beta\text{-}Mo_8O_{26}]^{4-}$ (b) and $[Cu_4O_6(pda)_4]$ (c), with gray atoms = C, blue = N, red = O, cyan = Mo, pink = Cu, and white = H.

clusters are formed from eight face- and edge-sharing MoO_6 octahedra, as described previously.[31] These clusters are bridged to four $[Cu(pda)]_4^{4+}$ tetramers through six terminal O atoms, while each $[Cu(pda)]_4^{4+}$ tetramer is bridged to four $[\beta\text{-}Mo_8O_{26}]^{4-}$ clusters. Overall, both types of clusters are connected into two-dimensional sheets that stack together down the *a* axis in an alternating arrangement, shown in Figure S2 (Supporting Information). Each Cu(I) cation is coordinated in a distorted tetrahedral geometry to two N atoms from two different pda ligands and to two O ligands from two $[\beta\text{-}Mo_8O_{26}]^{4-}$ clusters. The Cu–N/O bond distances are similar to those found in $Cu_2(pda)_3(ReO_4)_2$ and $Cu(bpy)ReO_4$.[19,20] The $[Cu(pda)]_4^{4+}$ can be viewed as two symmetric face-to-face $Cu_2(pda)_2^{2+}$ subunits, shown in Figure 1c, which are linked through pairs of oxo-bridging atoms from two molybdate clusters. This results in a face-to-face arrangement of the pda groups at $\pi-\pi$ stacking distances of ~3.2 Å, which is within the ranges of $\pi-\pi$ interactions in previously reported structures.[32,33]

The structures of $[Cu(en)_2]_2[\gamma\text{-}Mo_8O_{26}]$ (**II**) and $[Cu(o\text{-}phen)_2]_2[\alpha\text{-}Mo_8O_{26}]$ (**III**) have been reported previously[21,22] and are described only briefly. Compound **II** is comprised of $[Mo_8O_{26}]^{4-}$ octamolybdate clusters (γ-isomer) that are coordinated to two $Cu(en)_2^{2+}$ each at Cu–O distances of 2.46(1) Å, as shown in Figure 2. The $[\gamma\text{-}Mo_8O_{26}]^{4-}$ cluster

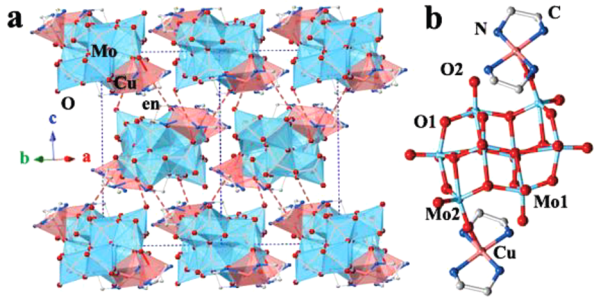

Figure 2. Polyhedral view of **II** (a); blue polyhedra are Mo-centered and pink are Cu-centered. The local $[CuO(en)_2]$ and $[\gamma\text{-}Mo_8O_{26}]^{4-}$ clusters (b), with gray atoms = C, blue = N, red = O, cyan = Mo and pink = Cu.

consists of two pairs of MoO_6 octahedra that are edge-sharing with two MoO_5 trigonal bipyramids, and capped by two additional MoO_6 octahedra. Each $Cu(en)_2^{2+}$ unit is also coordinated more weakly to a terminal oxygen ligand of another octamolybdate cluster at a longer Cu–O distance of 2.98(1) Å, labeled as dashed lines in Figure 2. These weaker interactions connect the clusters into a three-dimensional framework. The crystalline structure of **III** is that of a molecular solid, consisting of discrete $[Cu_2(o\text{-}phen)_4(\alpha\text{-}Mo_8O_{26})]$ clusters, shown in Figure 3. The $[Mo_8O_{26}]^{4-}$ cluster (α-

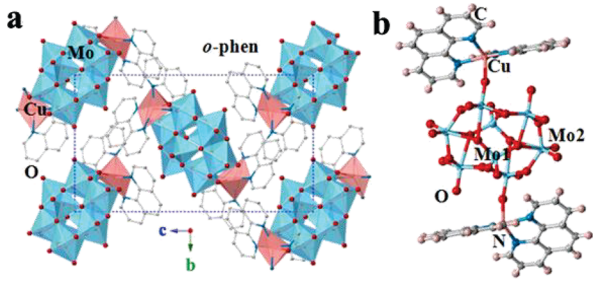

Figure 3. Polyhedral overview of **III** (a); blue polyhedra are Mo-centered and pink are Cu-centered. The local $[CuO(o\text{-}phen)_2]$ and $[\alpha\text{-}Mo_8O_{26}]^{4-}$ clusters (b), with gray atoms = C, blue = N, red = O, cyan = Mo, pink = Cu, and smaller cyan spheres = H.

isomer) consists of six edge-sharing MoO_6 octahedra and two MoO_4 tetrahedra. Two $Cu(o\text{-}phen)_2$ complexes coordinate to terminal oxygen atoms at opposite sides of the cluster at Cu–O distances of 2.19(2) Å. The next closest Cu–O distance between clusters is 4.05(6) Å.

Thus, in contrast to the extended two-dimensional structure of **I**, both **II** and **III** form as molecular solids with discrete (or nearly discrete) clusters. This structural difference arises from

dx.doi.org/10.1021/ic402910a | Inorg. Chem. 2014, 53, 3464–3470

the chelating ethylenediamine and *o*-phenanthroline ligands that block the bridging of Cu to multiple octamolybdate clusters. Pyridazine is a nonchelating ligand and results in a two-dimensional structure. Further, in contrast to compound **I** that contains Cu(I) cations, both **II** and **III** contain Cu(II) cations. These differences in the copper oxidation states and structural connectivities are found to significantly impact the resulting bandgap sizes, their solubilities in aqueous solutions, and photocatalytic activities of each of these hybrids, as described below.

Optical Band-Gap Sizes and Electronic Structures. The optical bandgap sizes of $[Cu(pda)]_4[\beta\text{-}Mo_8O_{26}]$ (**I**), $[Cu(en)_2]_2[\gamma\text{-}Mo_8O_{26}]$ (**II**), and $[Cu(o\text{-}phen)_2]_2[\alpha\text{-}Mo_8O_{26}]$ (**III**) were characterized by UV−vis diffuse reflectance techniques. Shown in Figure 4 are Tauc plots indicating the direct and

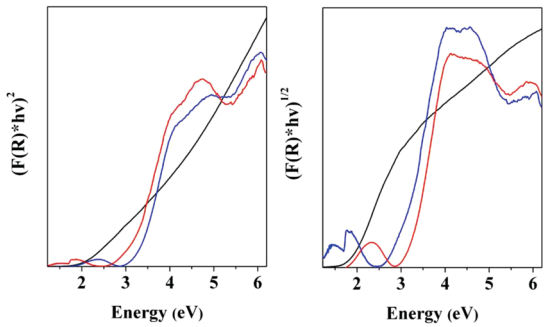

Figure 4. Tauc plots of $[F(R)h\nu]^n$ vs $[h\nu]$ for the direct and indirect bandgap sizes, n = 2 (left) and n = 1/2 (right), respectively, of **I** (black), **II** (blue), and **III** (red). The jump in the data at ∼1.8 eV arises from a change in detector at that wavelength.

indirect bandgap transitions for each. Both **II** and **III** exhibit similar (to within ∼0.1 eV) indirect and direct bandgap transitions of ∼3.0 to ∼3.1 eV. These molecular solids exhibit very little band dispersion in *k*-space, and thus the lowest-energy bandgap transition for each is expected to be direct. In addition, these exhibit lower-energy absorption peaks centered at ∼2.4 and ∼1.6 eV for **II** and **III**, consistent with the purple and green colors (complementary to the absorption wavelength) of these crystals, respectively. These absorption peaks arise from the d-to-d transitions on the Cu(II) cations. The relatively higher-energy d-to-d orbital transition in **II** arises from the distorted square-pyramidal geometry of Cu(II). In contrast, the Tauc plots of **I** exhibit a significantly lower-energy indirect bandgap transition of ∼1.8 eV, and a slightly higher direct transition at ∼2.0 eV. This is consistent with the deep brownish-red color of the crystals. Also, there is no detectable low-energy absorption peak in **I** arising from d-to-d transitions, as the structure contains Cu(I) cations with filled $3d^{10}$ orbital configurations.

The electronic origin of the significantly smaller bandgap size of **I**, compared to **II** and **III**, was investigated by density functional theory calculations of their electronic structures. The atomic contributions to the lowest-energy conduction band states were calculated and are plotted in Figure 5. The lowest-energy unoccupied crystal orbitals are found to consist of the empty molybdenum 4d orbitals located within the octamolybdate clusters (Figure 5A) that are mixed with smaller contributions from the oxygen 2p orbitals (green-shaded electron density) via $d(\pi)-p(\pi)$ antibonding interactions. The next four unoccupied bands, at ∼0.1 to ∼0.4 eV higher

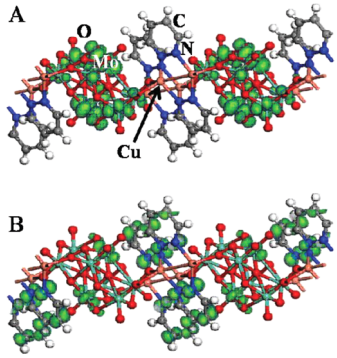

Figure 5. Calculated electron-density plots (green shading) for **I** of the lowest unoccupied crystal orbitals in the conduction band (A) and the next four higher-energy unoccupied crystal orbitals in the conduction band (B). These are overlaid on two-dimensional layers of the structure.

in energy, consist primarily of the ligand-based π^* states and a small amount from one Mo 4d orbital, shown in Figure 5B. However, electrons excited into these higher-energy bands would rapidly thermalize to the band edge states that are localized on the $[\beta\text{-}Mo_8O_{26}]^{4-}$ clusters, thus providing a driving force for charge separation in the excited state. The crystal orbitals at the edge of the valence band, shown in Figure 6

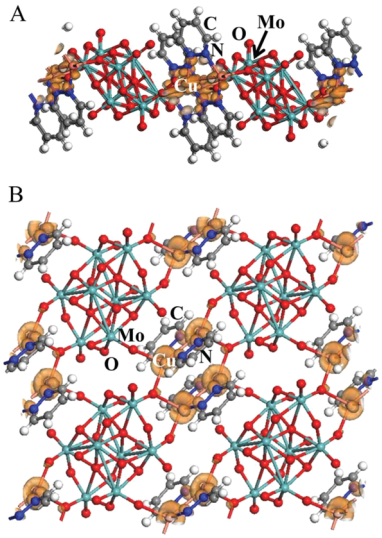

Figure 6. Calculated electron-density plots (orange shading) for **I** of the highest occupied crystal orbitals in the valence band, shown projected down the two-dimensional layer (A), and perpendicular to the layer (B). Atom types are labeled on each.

(orange-shaded electron density), are found to primarily consist of contributions from the Cu $3d^{10}$ orbitals. These are mixed with smaller contributions from the N 2p orbitals of the pda ligands via $d(\sigma)-p(\sigma)$ antibonding interactions. The electronic excitation between the valence and conduction band edges can be viewed as primarily a Cu(I)-to-Mo(VI) charge transfer, as well as Cu(I)-to-ligand at slightly higher energies. These results are consistent with our prior investigations involving the combination of two transition metals with filled d^{10} (i.e., Ag(I) or Cu(I)) and empty d^0 (i.e., Re(VII) or Nb(V)) electronic configurations. These mixed-metal systems show significantly decreased bandgap sizes, which increases their range of light absorption for use in solar energy applications.[7,11,12]

dx.doi.org/10.1021/ic402910a | *Inorg. Chem.* 2014, 53, 3464−3470

Photocatalytic Activities for Water-Splitting Reactions. The heterogeneous photocatalytic activities of **I**, **II**, and **III** were evaluated under visible and/or ultraviolet irradiation in (a) deionized water for total water splitting, and (b) in aqueous methanol solutions for water reduction to hydrogen. In the visible range of wavelengths, only **I** exhibited bandgap light absorption, whereas **II** and **III** only showed small absorption peaks originating from the Cu(II)-based d-to-d transitions. Accordingly, only **I** was found to show visible-light-driven photocatalytic activity in pure water with no sacrificial reagents or cocatalysts, with the detection of only trace amounts of hydrogen. Powder X-ray diffraction was used to confirm that **I** remains stable under each of these photocatalysis testing conditions (see the Supporting Information). Using only visible-light irradiation (420−800 nm) at a high power density of ∼1.0 W/cm^2, a photocatalytic rate of ∼90.0 μmol O_2 g^{-1} h^{-1} was measured over the course of two 3 h testing periods, as shown in Figure 7c. Recovery of the photocatalytic activity was obtained after resuspending the powder of **I** into a fresh aqueous solution. The turnover frequency per $[Mo_8O_{26}]^{4-}$ cluster was calculated to be ∼36 h^{-1}, based on its measured specific surface area of 1.5 m^2/g and the average density of surface clusters calculated for various planes of the crystal structure. Under both ultraviolet and ultraviolet and visible light irradiation, shown in Figure 7a, the photocatalytic activity of **I** in 20% methanol aqueous solution was measured to be ∼316 μmol H_2 g^{-1} h^{-1}, with a turnover frequency of ∼142 h^{-1}. Moreover, the rate was significantly enhanced to ∼471 μmol H_2 g^{-1} h^{-1}, with a turnover frequency of ∼193 h^{-1} after loading additional 1 wt % Pt cocatalyst on the surface of **I**, as shown in Figure 7b. Each of these rates declined over the course of several hours, but which could be recovered by drying and resuspending the crystalline particles in a fresh aqueous solution. Although several polyoxomolybdate compounds have recently been reported to be active for dye degradation,[14−16] only one recent example containing the octamolybdate cluster is known to be active for hydrogen production, with a reported rate of ∼0.78 μmol h^{-1} under ultraviolet irradiation.[34] For condensed metal-oxide photocatalysts (i.e., not containing ligands), rates for the production of oxygen and/or hydrogen under visible-light irradiation can vary significantly over the range of tens to thousands of micromoles per gram per hour, depending on the specific metal-oxide (e.g., $AgNbO_3$ and WO_3),[35] the irradiation intensity, and the use of cocatalysts and/or sacrificial reagents. Recently, we reported the first example of a metal-oxide/organic hybrid, $Mn(bpy)V_4O_{11}(bpy)$, that is photocatalytically active for total water splitting under visible-light irradiation with a rate of ∼21 μmol $H_2/^1/_2O_2$ g^{-1} h^{-1}.[36] Under comparable conditions, **I** exhibits higher visible-light photocatalytic activities.

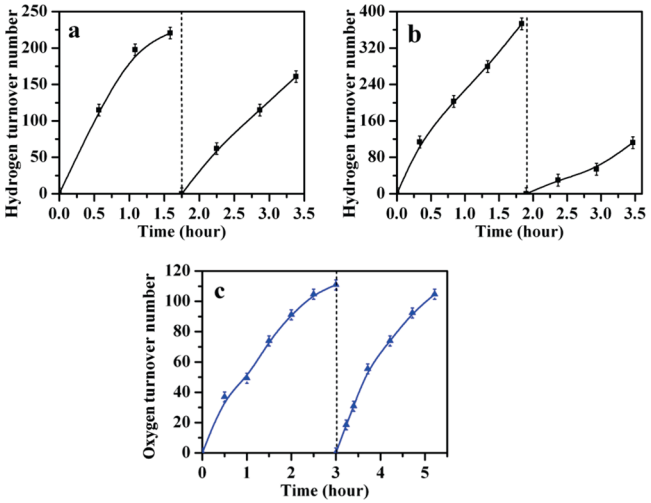

Figure 7. Photocatalytic activities per $[Mo_8O_{26}]^{4-}$ surface clusters in **I** at a radiant power density of 1 W/cm^2 (∼10 mg). Testing conditions for hydrogen production included ultraviolet and visible-light irradiation in a 20% aqueous methanol solution ((a) = pure catalyst; (b) = with a 1 wt % Pt surface cocatalyst), and for oxygen production included only visible light and deionized water (c).

Both **II** and **III** were also investigated for their photocatalytic activities in aqueous solutions. However, **II** decomposed under these conditions into partially reduced molybdate phases containing ammonium cations, as found by powder X-ray diffraction. The ethylenediamine ligand was not stable under irradiation and likely served to reduce the molybdenum cations within the octamolybdate cluster. Photocatalysis measurements of **III** under ultraviolet light in aqueous methanol solutions showed that it slowly dissolved over the course of several hours (up to ∼90 mg/L). Concomitantly, while **III** showed almost no photocatalytic activity at the start of the measurements, it exhibited an accelerating activity for hydrogen production owing to its dissolution over time. The rates of photocatalytic activity stabilized after ∼2−3 h. The activity of **III** was found to originate from the dissolved $[Cu_2(o\text{-phen})_4(\alpha\text{-}Mo_8O_{26})]$ molecular clusters, as the photocatalytic rates measured for the solution were the same with or without the presence of the solid powder. A saturated solution of the dissolved clusters of **III** was prepared by full-spectrum irradiation of a powdered sample for 25 h in a 20% aqueous methanol solution, followed by centrifuging the remaining powder and decanting off the supernatant (∼3.2 mg dissolved). As shown in Figure 8, an aqueous methanol solution of **III** showed a high photocatalytic activity for hydrogen production of ∼4700 μmol H_2·g^{-1} h^{-1}. During the course of a 17 h experiment, ∼246 μmol of hydrogen was produced from 1.56 μmol of **III** (dissolved), with a total turnover number of ∼157 and a turnover frequency per $[Cu_2(o\text{-phen})_4(\alpha\text{-}Mo_8O_{26})]$ cluster of ∼9 h^{-1}. The products of methanol oxidation included formaldehyde and methyl formate,

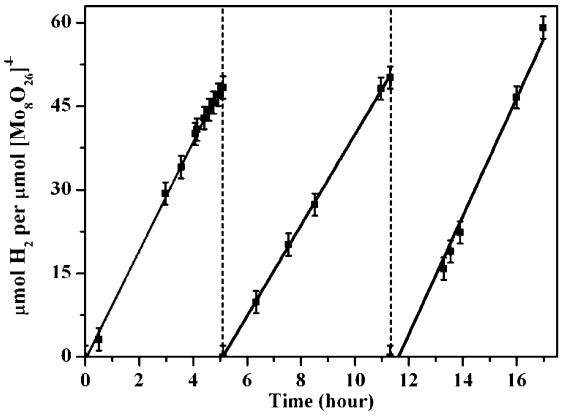

Figure 8. Homogeneous photocatalytic hydrogen production for **III** (∼3.2 mg) dissolved in a 20% aqueous methanol solution (∼45 mL; no Pt cocatalyst) under ultraviolet and visible-light irradiation (at ∼1.0 W/cm^2).

dx.doi.org/10.1021/ic402910a | Inorg. Chem. 2014, 53, 3464−3470

confirmed by Tollen's test and gas chromatography, which decreased the pH of the resulting solution to ~3. Hydrogen gas was the only gas product detected from the photocatalytic reduction reaction.

The precipitation of the dissolved clusters of **III** results in a brown powder that is amorphous by powder X-ray diffraction, as shown in Figure S13 (Supporting Information). Approximately 1.35 mg of this amorphous powder was redissolved into aqueous methanol and exhibited photocatalytic activity for hydrogen production of ~8670 μmol $H_2 \cdot g^{-1}$ h^{-1} with a turnover frequency of ~17 h^{-1}, shown in Figure 9. More than

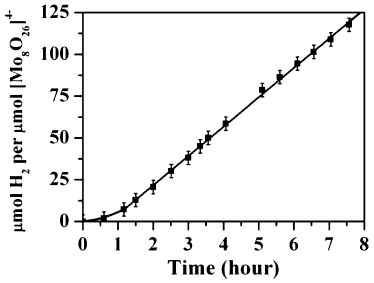

Figure 9. Photocatalytic hydrogen production of the redissolved precipitant from **III** under ultraviolet and visible-light (250−800 nm) irradiation in 45 mL of a 20% methanol aqueous solution.

78 μmol of hydrogen evolved with a total turnover number of ~118 after an 8 h reaction time. During the initial dissolution of the clusters, the color of the solid powder changed from green to brown, indicating a possible change in structure or in oxidation states. The UV−vis diffuse reflectance of the brown amorphous powder shows a new broad absorption edge that emerges beginning at ~1.7 eV, shown in Figure 10. Mass

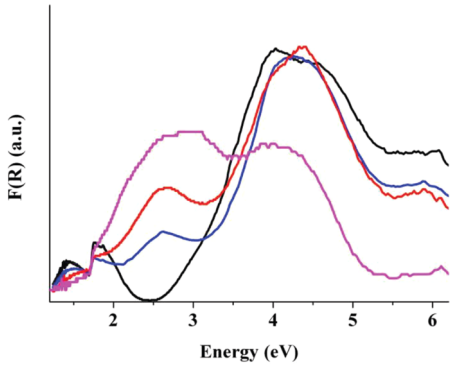

Figure 10. UV−visible diffuse reflectance spectra of **III**: as-synthesized (black), after photocatalytic reaction under ultraviolet irradiation for 12 h (blue), 25 h (red), and the brown precipitant from solution (pink). The jump in the data at ~1.8 eV corresponds to a change in the instrument detector at that energy.

spectrometry measurements confirmed the presence of the $[Cu(o\text{-phen})_2]_2[\alpha\text{-}Mo_8O_{26}]$ clusters in **III**. However, after irradiation of **III** by ultraviolet light in methanol solution, the mass spectrometry data show primarily protonated $[\alpha\text{-}Mo_8O_{26}]^{4-}$ species in solution. Further, the electron paramagnetic resonance data exhibit a decreased amount of Cu(II) cations in the precipitant. This suggests the reduction of Cu(II) to Cu(I) in the solution of **III** while under ultraviolet irradiation, resulting in a decreased bandgap size that is similar in origin to that for **I** (i.e., d^{10}-to-d^0 electronic transitions). Subsequently, during the dissolution of **III**, a significant fraction of the Cu(I)/Cu(II) cations become detached from the octamolybdate clusters, especially as a result of the solution becoming increasingly acidified owing to the products of methanol oxidation. This is consistent with the electronic structure calculations that suggest the origin of the photocatalytic activity for water reduction is from the electrons excited within the $[Mo_8O_{26}]^{4-}$ clusters.

A comparison of the photocatalytic activities of **I** (heterogeneous) and **III** (homogeneous) yields several interesting insights. Whereas **I** is active under visible-light irradiation owing to a Cu(I)-to-Mo(VI) charge transfer, **III** is active under only ultraviolet irradiation that instead stems from the higher-energy excitation from the oxide ligands to Mo(VI). The molecular structure of **III** renders it more soluble in aqueous solutions, ultimately leading to the detachment of the Cu cations from the octamolybdate clusters. When tested under similar conditions, the dissolved octamolybdate clusters from **III** exhibit the higher photocatalytic rates per gram for hydrogen production of ~4700 μmol H_2 g^{-1} h^{-1}, compared to ~316 μmol H_2 g^{-1} h^{-1} for **I**. However, **III** shows lower turnover frequencies per $[\alpha\text{-}Mo_8O_{26}]^{4-}$ cluster at ~9 h^{-1}, compared to **I** of ~142 h^{-1}. In homogeneous photocatalysis, all $[\alpha\text{-}Mo_8O_{26}]^{4-}$ clusters are dissolved in solution and can function as catalyst sites for water reduction. Therefore, although each dissolved cluster from **III** exhibits a relatively lower turnover frequency, the net sum of all of their individual contributions leads to a higher overall photocatalytic rate. In heterogeneous photocatalysis, by contrast, only the exposed surface $[\beta\text{-}Mo_8O_{26}]^{4-}$ clusters can function as catalyst sites for water reduction. Thus, while the turnover frequencies of surface $[\beta\text{-}Mo_8O_{26}]^{4-}$ clusters are significantly higher, the total activity arises from the sum of the significantly fewer number of surface sites, yielding a smaller overall photocatalytic rate for hydrogen production. However, the difference in photocatalytic turnover frequencies is not necessarily a result of the $[\beta\text{-}Mo_8O_{26}]^{4-}$ cluster in **I** versus the $[\alpha\text{-}Mo_8O_{26}]^{4-}$ cluser in **III**. The smaller bandgap size and broader absorption range of **I** can partly explain these higher turnover frequencies. In addition, the absorption of light and the generation of excited electrons occur throughout the structure of **I**, resulting in a greater number of electrons that funnel toward a smaller number of photocatalytically active surface sites.

CONCLUSION

The relationships between the structures, optical bandgap sizes, and photocatalytic activities of three copper−octamolybdate hybrid solids have been investigated, including $[Cu(pda)]_4[\beta\text{-}Mo_8O_{26}]$ (**I**), $[Cu(en)_2]_2[\gamma\text{-}Mo_8O_{26}]$ (**II**), and $[Cu(o\text{-phen})_2]_2[\alpha\text{-}Mo_8O_{26}]$ (**III**). The two-dimensional connectivity of **I** is achieved by bridging of the $[Cu(pda)]_4^{4+}$ tetramers to four neighboring $[\beta\text{-}Mo_8O_{26}]^{4-}$ octamolybdate clusters. The chelating organic ligands in **II** and **III** result in simpler molecular structures. The optical bandgap size of **I** was shown to occur within the visible-light energy range at ~1.8 eV owing to the incorporation of Cu(I) cations within its structure, whereas **II** and **III** are comprised of Cu(II) cations and exhibit bandgap sizes of ~3.1 and ~3.0 eV, respectively. The smaller bandgap size of **I** originates primarily from an electronic transition between the filled Cu(I) $3d^{10}$ orbitals and the empty Mo(VI) $4d^0$ orbitals at the respective valence and conduction band edges. Without any cocatalyst, compound **I** exhibits visible-light photocatalytic activity for oxygen production at a rate of ~90

dx.doi.org/10.1021/ic402910a | Inorg. Chem. 2014, 53, 3464−3470

μmol O_2 g^{-1} h^{-1}, and for hydrogen production under ultraviolet light at a rate of ~316 μmol H_2 g^{-1} h^{-1} (10 mg sample; radiant power density of ~1 W/cm^2), respectively. Corresponding turnover frequencies per calculated surface cluster were ~36 and ~142 h^{-1}. By contrast, **II** decomposed during the photocatalysis measurements. The molecular clusters of **III** dissolved into aqueous methanol solutions under ultraviolet irradiation and exhibited homogeneous photocatalytic rates for hydrogen production of up to ~8670 μmol $H_2 \cdot g^{-1}$ h^{-1} and a turnover frequency per cluster of 17 h^{-1}. During the photocatalysis measurements, the dissolution of the clusters in **III** is found to occur with the reduction of Cu(II) to Cu(I), followed by subsequent detachment from the octamolybdate cluster.

■ ASSOCIATED CONTENT

Supporting Information

Tables of selected single-crystal X-ray refinement data, powder X-ray diffraction data, FT-IR spectra, mass spectrometry data, thermogravimetric analyses, X-ray photoelectron spectroscopy data, electron paramagnetic resonance data, and additional photocatalysis data. This material is available free of charge via the Internet at http://pubs.acs.org.

■ AUTHOR INFORMATION

Corresponding Author

*E-mail: Paul_Maggard@ncsu.edu.

Notes

The authors declare no competing financial interest.

■ ACKNOWLEDGMENTS

Assistance with the collection of single-crystal X-ray diffraction data (Dr. P. Boyle), X-ray photoelectron spectroscopy data (Prof. D. Dougherty), and mass spectra data (Drs. V. Kandhi and D. Lehman) is acknowledged. Financial support of this research is acknowledged from the Research Corporation for Science Advancement (P.M. is a Scialog Awardee), from the National Science Foundation (DMR-0644833), and the Department of Chemistry at North Carolina State University.

■ REFERENCES

(1) Osterloh, F. E. *Chem. Mater.* **2008**, *20*, 35−54.
(2) Fujishima, A.; Honda, K. *Nature* **1972**, *238*, 37.
(3) Joshi, U. A.; Palasyuk, A.; Arney, D.; Maggard, P. A. *J. Phys. Chem. Lett.* **2010**, *1*, 2719−2726.
(4) Kudo, A.; Miseki, Y. *Chem. Soc. Rev.* **2009**, *38*, 253.
(5) Choi, J.; King, N.; Maggard, P. A. *ACS Nano* **2013**, *7*, 1699−1708.
(6) Fuoco, L.; Joshi, U. A.; Maggard, P. A. *J. Phys. Chem. C* **2012**, *116*, 10490−10497.
(7) Joshi, U. A.; Maggard, P. A. *J. Phys. Chem. Lett.* **2012**, *3*, 1577−1581.
(8) Joshi, U. A.; Palasyuk, A.; Maggard, P. A. *J. Phys. Chem. C* **2011**, *115*, 13534−13539.
(9) Arney, D.; Hardy, C.; Greve, B.; Maggard, P. A. *J. Photochem. Photobiol., A* **2010**, *214*, 54−60.
(10) Hagrman, P. J.; Finn, R. C.; Zubieta, J. *Solid State Sci.* **2001**, *3*, 745−774.
(11) Hagrman, P. J.; Hagrman, D.; Zubieta, J. *Angew. Chem., Int. Ed.* **1999**, *38*, 2638−2684.
(12) Lin, H.; Maggard, P. A. *Inorg. Chem.* **2008**, *47*, 8044.
(13) Lin, H.; Maggard, P. A. *Cryst. Growth Des.* **2010**, *10*, 1323−1331.
(14) Zhang, Z.; Yang, J.; Liu, Y.-Y.; Ma, J.-F. *CrystEngComm* **2013**, *15*, 3843−3853.
(15) Kan, W.-Q.; Yang, J.; Liu, Y.-Y.; Ma, J.-F. *Dalton Trans.* **2012**, *41*, 11062−11073.
(16) Liu, B.; Yang, J.; Yang, G.-C.; Ma, J.-F. *Inorg. Chem.* **2013**, *52*, 84−94.
(17) Yin, Q.; Tan, J. M.; Besson, C.; Geletii, Y. V.; Musaev, D. G.; Kuznetsov, A. E.; Luo, Z.; Hardcastle, K. I.; Hill, C. L. *Science* **2010**, *328*, 342.
(18) Lv, H.; Geletii, Y. V.; Zhao, C.; Vickers, J. W.; Zhu, G.; Luo, Z.; Song, J.; Lian, T.; Musaev, D. G.; Hill, C. L. *Chem. Soc. Rev.* **2012**, *41*, 7572.
(19) Lin, H.; Maggard, P. A. *Inorg. Chem.* **2009**, *48*, 8940−8946.
(20) Lin, H.; Maggard, P. A. *Inorg. Chem.* **2007**, *46*, 1283−1290.
(21) DeBord, J. R. D.; Haushalter, R. C.; Meyer, L. M.; Rose, D. J.; Zapf, P. J.; Zubieta, J. *Inorg. Chim. Acta* **1997**, *256*, 165.
(22) Hagrman, P. J.; Zubieta, J. *Inorg. Chem.* **1999**, *38*, 4480.
(23) *SAINT*; Bruker AXS Inc.: Madison, WI, 2007.
(24) Sheldrick, G. *Acta Crystallogr., Sect. A* **2008**, *64*, 112.
(25) Kortüm, G. *Reflectance Spectroscopy: Principles, Methods, Applications*; Springer-Verlag: New York, 1969.
(26) Yu, J.; Kudo, A. *Adv. Funct. Mater.* **2006**, *16*, 2163.
(27) Zhang, Z.; Maggard, P. A. *J. Photochem. Photobiol., A* **2007**, *186*, 8−13.
(28) Clark, S. J.; Segall, M. D.; Pickard, C. J.; Hasnip, P. J.; Probert, M. I. J.; Refson, K.; Payne, M. C. *Z. Kristallogr. - Cryst. Mater.* **2005**, *220*, 567.
(29) Payne, M. C.; Teter, M. P.; Allan, D. C.; Arias, T. A.; Joannopoulos, J. D. *Rev. Mod. Phys.* **1992**, *64*, 1045.
(30) Monkhorst, H. J.; Pack, J. D. *Phys. Rev. B* **1976**, *13*, 5188.
(31) Bridgeman, A. J. *J. Phys. Chem. A* **2002**, *106*, 12151−12160.
(32) Eliseeva, S. V.; Mirzov, O. V.; Troyanov, S. I.; Vitukhnovsky, A. G.; Kuzmina, N. P. *J. Alloys Compd.* **2004**, *374*, 293.
(33) Sakai, K.; Kurashima, M. *Acta Crystallogr., Sect. E* **2003**, *59*, 411.
(34) Fu, H.; Qin, C.; Lu, Y.; Zhang, Z.-M.; Li, Y.-G.; Su, Z. M.; Li, W.-L.; Wang, E.-B. *Angew. Chem., Int. Ed.* **2012**, *51*, 7985−7989.
(35) Kato, H.; Kobayashi, H.; Kudo, A. *J. Phys. Chem. B* **2002**, *106*, 12441.
(36) Luo, L.; Maggard, P. A. *Cryst. Growth Des.* **2013**, *13*, 5282−5288.